A STUDY OF H₂ EMISSION IN THE BIPOLAR PROTO–PLANETARY NEBULA IRAS 17150−3224[1]

BRUCE J. HRIVNAK,[2] DOUGLAS M. KELLY,[3] KATE Y. L. SU,[3] SUN KWOK,[4] AND RAGHVENDRA SAHAI[5]

ABSTRACT

H₂ emission has been detected in the bipolar proto–planetary nebula IRAS 17150−3224 from the 1−0 $S(1)$, 1−0 $S(0)$, and 2−1 $S(1)$ transitions in the 2 μm region. Line ratios suggest that this emission is due to collisional excitation. High-resolution imaging with NICMOS on *HST* shows that the emission comes from four regions: clumps near the ends of the lobes (the brightest region), the lobes in general, a particular region outside the northwest lobe, and a faint loop in the equatorial region. Spatially resolved high-resolution spectra at 2.12 μm reveal that the H₂ 1−0 $S(1)$ line has a velocity width of about 35 km s^{-1} in the lobes, consistent with C-type shocks. The emission from the clumps in the lobes appears to arise from the impact of a fast wind with the slower moving material in the AGB wind.

Subject headings: circumstellar matter — infrared: stars — planetary nebulae: general — stars: AGB and post-AGB — stars: mass loss

Online material: color figures

1. INTRODUCTION

The identification of proto–planetary nebulae (PPNs), objects in transition between the asymptotic giant branch (AGB) and planetary nebula (PN) phases of stellar evolution, began in earnest two decades ago with the results of the *IRAS* mid-infrared survey. High-resolution imaging in the past decade with the *Hubble Space Telescope* (*HST*) has revealed that PPNs have a variety of shapes, most with a basic bipolar structure (Ueta et al. 2000; Su et al. 2001), but some appearing quadrupolar or multipolar (Sahai et al. 2005). Thus, the shaping of the basically spherical outflow from AGB stars into the complex morphologies seen in PN (Sahai & Trauger 1998; Balick & Frank 2002) begins during this transient PPN phase (lifetime of few thousand years; Blöcker 1995).

One can ask whether this shaping is imprinted on the initial AGB outflow or occurs later by the initiation of the fast wind that sweeps up the slow AGB outflow to form the PN (Kwok 1982; Balick 1987). This can be partially answered by the high-resolution images of PPNs, which in some cases show both large, circular, concentric arcs and bipolar lobes emanating from a dense torus. These suggest an initially spherical mass loss in which an asymmetry developed that led to the torus and lobes. Recent H₂ surveys of PPNs have shown the presence of shock-excited H₂ emission from bipolar PPNs with central stars of F–G spectral type (García-Hernández et al. 2002; Kelly & Hrivnak 2005).

These studies point to the presence of a collimated wind in bipolar PPNs that occurs early in the evolution from cool central stars to the hotter central stars found during the PN phase. Several high-resolution H₂ spatial and spectral studies of PPNs

have recently been published that bear on this question. These include an H₂ imaging study of AFGL 2688 (Sahai et al. 1998), a spatial and spectral study of AFGL 618 (Cox et al. 2003), a H₂ spectroscopic study of AFGL 2688 and AFGL 618 (Kastner et al. 2001) and, just recently, four other PPNs (Davis et al. 2005).

In this paper we present the results of a detailed, high-resolution H₂ emission study of the bipolar PPN IRAS 17150−3224 (AFGL 6815S; "Cotton Candy Nebula"). The nebula is viewed approximately edge-on, with a dark lane obscuring the central star in visible light (Kwok et al. 1996). It also shows a series of circumstellar arcs and two pairs of oppositely directed "searchlight beams" projected along the edges of the lobes (Kwok et al. 1998; Ueta et al. 2000). In visible light it thus appears very similar to AFGL 2688. However, in the near-infrared the central star of IRAS 17150−3224 is seen between the lobes (Su et al. 2003), in contrast to the obscured central star of AFGL 2688. We begin with a presentation of the H₂ spectrum, then the high-resolution H₂ image, and then spatially resolved high-resolution H₂ spectra. The excitation mechanism and the properties of the emitting regions are then discussed. We conclude with a discussion of the structure of the nebula.

2. H₂ SPECTRUM

Medium-resolution spectroscopic observations were obtained in the 2 μm region on 1999 June 30 and July 1, using the Steward Observatory 2.3 m telescope on Kitt Peak. The cryogenically cooled, long-slit, near-infrared spectrograph FSpec was used, and the resulting spectra have a resolution ∼2600. The spectrograph slit had a size of 2″.4 × 86″ projected onto the sky and was oriented approximately east-west.

Three slightly different grating rotations (λ_c = 2.14, 2.21, and 2.28 μm) yielded adjoining spectra with a slight wavelength overlap; these were combined to produce a continuous spectrum from 2.10 to 2.32 μm. The total observing times in each of the three wavelength regions was 1080, 1080, and 720 s, respectively. Dark current and flat-field images were taken and used to correct the target observations. Reduction was carried out using IRAF.[6]

[2] Department of Physics and Astronomy, Valparaiso University, Valparaiso, IN 46383; bruce.hrivnak@valpo.edu.
[3] Steward Observatory, The University of Arizona, Tucson, AZ 85721; dkelly@as.arizona.edu, ksu@as.arizona.edu.
[4] Department of Physics, University of Hong Kong, Hong Kong, China; and Department of Physics and Astronomy, University of Calgary, Calgary, T2N 1N4 Canada; sunkwok@hku.hk.
[5] JPL/Caltech, 4800 Oak Grove Drive, Pasadena, CA 91109; raghvendra.sahai@jpl.nasa.gov.

[6] IRAF is distributed by the National Optical Astronomical Observatories, operated by the Association for Universities for Research in Astronomy, Inc., under contract to the National Science Foundation.
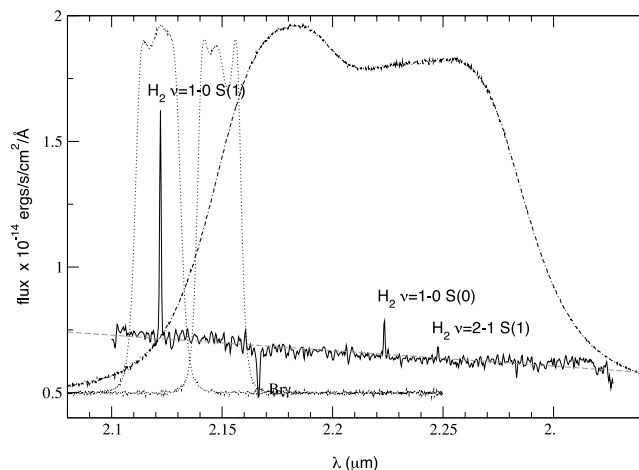
Fig. 1.—Spectrum of IRAS 17150−3224, showing the H_2 emission features. Shown also are the *HST* NICMOS F212N, F215N, and F222M filter profiles, shifted to 0.5 and scaled relatively along the *y*-axis. [*See the electronic edition of the Journal for a color version of this figure.*]

The sky contribution was removed by subtracting adjacent sky images. The wavelength scale was determined from the OH airglow lines present in the spectra before sky subtraction. Telluric absorption lines were removed by ratioing the spectra with those of bright reference stars at similar airmasses. Since G3 V and F9 V reference stars were used to ratio the 2.14 μm and 2.21 μm spectra, care had to be taken to correct for absorption features intrinsic to the reference spectra. This was done by multiplying by a slightly modified solar spectrum. To restore the continuum shape, the resulting spectrum was multiplied by the ratio of reference star and solar temperature blackbody curves. Flux calibration was carried out using the known *K*-band magnitude of IRAS 17150-3224. For more details of the spectral reduction procedure, see Kelly & Hrivnak (2005).

The seeing was not very good during the observations, so we made no attempt to place the slit along different regions of the nebula. The slit was simply placed through the middle of the image as seen by the *H*-band guiding camera. Thus the spectrum does not include the entire nebula, and in particular, the ends of the lobes were partly excluded.

The 2 μm spectrum of IRAS 17150−3224 is displayed in Figure 1. It shows a very strong emission line due to H_2 at 2.122 μm [$\nu = 1-0$ $S(1)$], with additional H_2 emission lines at 2.223 μm [$\nu = 1-0$ $S(0)$] and 2.248 μm [$\nu = 2-1$ $S(1)$]. H_2 emission at 2.154 μm [$\nu = 2-1$ $S(2)$] and 2.201 μm [$\nu = 3-2$ $S(3)$] was not detected. Since the spectral type of the central star is G2 I (Hu et al. 1993), the strong Brγ absorption at 2.166 μm is expected (Kelly & Hrivnak 2005). The strengths of the three H_2 lines were measured to be 7.8×10^{-14} ergs cm^{-2} s^{-1} [$1-0$ $S(1)$], 1.3×10^{-14} ergs cm^{-2} s^{-1} [$1-0$ $S(0)$], and 0.6×10^{-14} ergs cm^{-2} s^{-1} [$2-1$ $S(1)$]. However, these values are only approximate. They are slight overestimates of the observed line strengths, since the flux calibration was based on the *K*-band magnitude of the object and some of the continuum flux from the ends of the lobes was not included in the slit. On the other hand, as will be shown later, significant H_2 emission from the ends of the lobes was not included in the slit. The H_2 is extended as compared to the continuum, with a FWHM in spatial extent of 3″ and a full extent of 7″.

3. H_2 IMAGE

High-resolution near-infrared imaging observations of IRAS 17150−3224 were obtained on 1998 August 16 with the *Hubble*

Space Telescope (*HST*) under General Observer program ID 7840 (PI: Kwok). The Near-Infrared Camera and Multiobject Spectrometer (NICMOS) camera 2 (NIC2) was used, which has a resolution of 0″076 × 0″075 pixel^{-1} and a field of view of 19″5 × 19″3. Observations were made with a narrowband H_2 filter (F212N) and its adjacent continuum filter (F215N) for the purpose of distinguishing the H_2 $1-0$ $S(1)$ emission from the stellar continuum and scattered starlight. The data were taken in the multiple nondestructive mode (MULTIACCUM) to obtain a high dynamic range without saturating the data. Three sets of observations were made through each filter, and in each set the target was imaged three successive times at different positions of the NIC2 array, using a predefined dither pattern. The final combined exposure time in each filter was 816 s.

The data were recalibrated using the *HST* archival On-the-Fly Reprocessing system, which provides recalibration using the most up-to-date reference files for bias, dark subtraction, and flatfield correction (NICMOS calnica pipeline). The individual files were then corrected for the pedestal effect using the IRAF STSDAS pedsub task to flatten the sky value in the four quadrants of the NIC2 array. We then mosaicked the dithered images using two different methods: (1) the centroiding of field stars and (2) the drizzle technique. We used the IDL-based software package IDP3 (Schneider & Stobie 2002) to register the nine dithered images using centroids of field stars, and then median combined the images. We also combined the nine images using the IRAF STSDAS dither package with the parameters suggested in the *HST Dither Handbook* (Koekemoer et al. 2002). The two images mosaicked using the different methods show no significant differences (<1%) in background noise and photometry of field stars. Since the drizzle technique can also correct geometric distortion and maximize spatial sampling, we therefore adopted the drizzled mosaics for further analysis.

The resultant flux-calibrated F212N and F215N images, with all thermal background removed, are displayed in Figures 2*a* and 2*b*. They appear to be quite similar. Most of the light is coming from the central star and the region between the lobes, with some fainter light coming from the ends of the lobes and some clumps in the lobes. This similarity implies that most of the light in the F212N image is actually scattered starlight. Thus, the H_2 emission from this object is not as relatively strong as the emission detected in AFGL 2688, in which the H_2 flux could easily be distinguished from the continuum (Sahai et al. 1998). This is even more the case in PNs, where the continuum is very low and the H_2 emission can be traced directly by the H_2 image (Kastner et al. 1996). To produce an image of IRAS 17150−3224 showing only H_2 emission requires the careful removal of this scattered light, which can be accomplished through the subtraction of an appropriately scaled image of the adjacent continuum.[7]

Although the images with the two filters were obtained with the same exposure times, one cannot get a resultant H_2 image by simply subtracting them directly, because of differences in the filter profiles, detector responses, and source continuum shape. We examined several different ways to calculate the appropriate scale factor to use when subtracting the adjacent continuum image. The first thing done was to convert to flux-calibrated images using the flux calibration values for the two filters (PHOTFLAM; see Table 1).

---

[7] In deriving an H_2 image of the young PN NGC 7027 from F212N and F215N observations, Latter et al. (2000) needed to correct both the F212N image for the relatively strong He I emission line at 2.113 μm and the F215N image for the strong Brγ emission line; neither of these lines appears in emission in IRAS 17150−3224, and they need not be considered here.
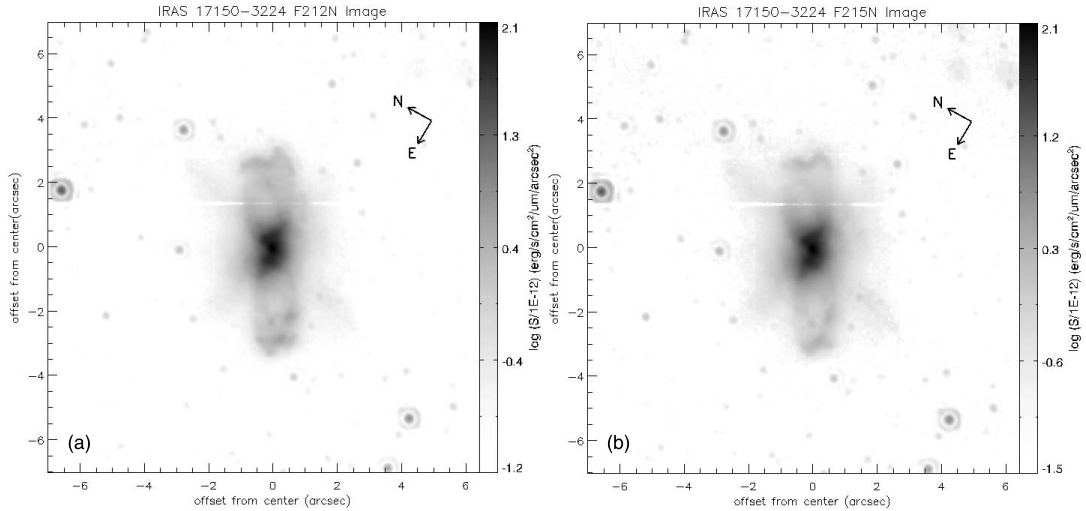
Fɪɢ. 2.—Flux-calibrated images of IRAS 17150−3224: (*a*) F212N and (*b*) F215N, both in reversed, logarithmic scale.

To include the correction for the source spectral shape, we examined two different ways to calculate an appropriate scale factor to use for the adjacent continuum image. The first involved an additional scaling based on the spectral continuum shape of IRAS 17150−3224 within the two filters, which resulted in a scale factor of 1.0242. The second involved scaling based on the observed flux of the field stars in the images, and resulted in a scale factor of 1.045 ± 0.015. These two methods lead to quite similar H$_2$ images for the nebula. This is discussed in more detail in the Appendix. We adopted the scaling factor based on the fit to the spectral shape of the central star in the nebula. This is shown in Figure 3.

The H$_2$ emission detected in the nebula is seen in four distinct distributions. Bright clumps of emission are seen near the ends of the two lobes. Faint emission is also seen coming from the lobes in general. There is a particular, faint region of emission along the southwestern edge outside the northwest lobe. In addition, there also appears to be faint emission (∼5–10 σ_{sky}) from a partial loop extending northeast from the waist region; this loop feature was first identified in recent *H* and *K* images obtained with the *HST* (Su et al. 2003). The latter two H$_2$ regions will appear more clearly, with labels, on some of the later figures.

The approximate slit position of the FSpec spectrograph is superimposed in Figure 3*a*. Integrating the H$_2$ emission within this slit area results in an H$_2$ flux of 5.8×10^{-14} ergs cm^{-2} sec^{-1}. This is reasonably close to the observed (§ 2) value, now more properly scaled by the fact that only about 92% of the *K*-band flux is calculated to pass through the FSpec slit, of 7.2×10^{-14} ergs cm^{-2} s^{-1}.

4. HIGH-RESOLUTION H$_2$ SPECTRUM

Long-slit, high-spectral resolution observations of IRAS 17150−3224 were made in the H$_2$ 1–0 *S*(1) line at 2.1218 μm, using the echelle spectrograph Phoenix (Hinkle et al. 1998) on the 4 m telescope at Kitt Peak National Observatory on 2000 June 14–16. The spectral coverage was 1280 km s^{-1}, the dispersion was 1.27 km s^{-1} pixel^{-1}, and the resolution was 6 km s^{-1}. The slit width was 0″.74, and the plate scale was 0″.186 pixel^{-1}. Spectra were obtained in four slit positions, three with the slit oriented parallel to the major axis of the nebula (P.A. = 123°): one through the star and two offset north and south by 0″.84, and one through the star perpendicular to the nebular axis (P.A. = 33°; see Table 2). These are illustrated in Figure 3*b*, where we have labeled the slit positions as L (left), C (center), R (right), and S (stellar) to aid in the following description. The source was moved along the slit between exposures.

The spectra were reduced using IRAF. Spectra were differenced to remove contributions from dark current and from sky emission. If necessary, the reference spectrum was scaled upward or downward by a few percent to improve the cancellation of sky lines. The spectra were flat-fielded using observations of an internal tungsten filament lamp. The images were masked for bad pixels and trimmed. The difference images were then aligned and co-added. The resulting position-velocity images were rotated to align the spectral axis with the columns. OH airglow lines at 2.11766 and 2.12325 μm (vacuum wavelengths) were used to wavelength calibrate the data, and velocities were corrected to the heliocentric system. The zero point of the spatial

TABLE 1
Pʜᴏᴛᴏᴍᴇᴛʀɪᴄ Cᴀʟɪʙʀᴀᴛɪᴏɴ Vᴀʟᴜᴇs

Filter	λ_c (μm)	$\Delta\lambda$ (μm)	PHOTFLAM (ergs cm$^{-2}\mu$m^{-1}DN^{-1})	PHOTFNU (Jy s DN^{-1})	ZP (Vega) (Jy)	PSF FWHM[a] (arcsec)
F212N	2.1213	0.0208	2.4272E-14	3.6432E-5	664.7	0.20
F215N	2.1487	0.0203	2.5533E-14	3.9323E-5	645.1	0.21
F222M	2.2182	0.1455	3.1754E-15	5.2116E-6	610.4	0.18

Nᴏᴛᴇ.—The photometric calibration values were taken from the online NICMOS photometry performance for pre-NICMOS Cooling System installation (operating temperature of detector ∼62 K).

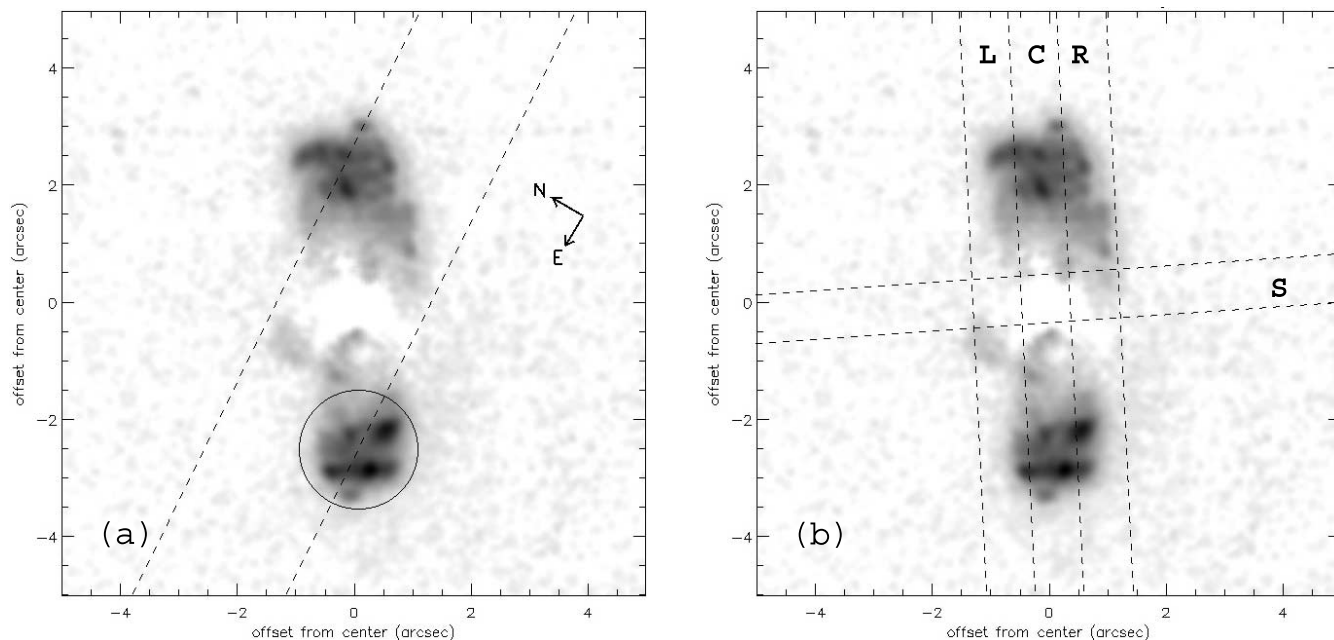[a] Based on a Gaussian fit to the observed field stars.

Fig. 3.—(a) Continuum-subtracted H_2 image of IRAS 17150−3224 with the approximate slit position of the medium-resolution spectra superimposed (*dashed lines*). Also delineated is an aperture around the strongest emission clumps in the southeast lobe that was used to measure the emission in this region (see Appendix). (b) H_2 image of IRAS 17150−3224 showing the positions of the slits for the four high-resolution H_2 spectra. The four spectra are labeled as L (left), C (center), R (right), and S (stellar).

scale was determined based on the centroid of the continuum flux. The IRAF `background` routine was used to average pixels within user-defined apertures blueward and redward of the H_2 line, and to subtract this flux on a column-by-column basis. This operation removed residual sky and subtracted the stellar continuum, leaving the H_2 emission. The resulting position-velocity diagrams are shown in Figure 4. Positive positions are along the northwest lobe. The data are not flux calibrated.

Only a single exposure was obtained with the slit angle orthogonal to the polar axis, and this on a different night from the others. To remove the sky emission in this case, the spectrum of the PPN IRAS 17441−2441, which was observed immediately after IRAS 17150−3224, was used. With only a single spectral image, it was not possible to identify cosmic rays during the co-adding process, so the IRAF task `cosmicrays` was used for the threshold identification and removal of cosmic rays. Otherwise, the reduction process was identical to that used for the other spectra. However, the final position-velocity spectrum was boxcar smoothed by a factor of 5 along each axis to bring up the contrast of the fainter emission against the background.

In spite of the compact appearance of the nucleus in the H_2 image, continuum flux appeared in all four slit positions. Furthermore, the relative fluxes from the slit positions are also not fully consistent with the H_2 image. Thus, it seems that the three polar spectra are not quite as distinctly separated spatially as

TABLE 2
High-Resolution H_2 Observing Log

Date	P.A. (deg)	Position	t_{exp} (min)	Number of Observations
2000 Jun 14	123	C − through star	30	3
2000 Jun 15	33	S − through star	30	1
2000 Jun 16	123	L − 0″.84 N of star	30	2
2000 Jun 16	123	R − 0″.84 S of star	30	2

Figure 3*b* indicates. Although an autoguider maintained the pointing during the 30 minute integrations, the seeing during the Phoenix observations was ∼1″ and this apparently led to some imaging smearing in the slits.

While the H_2 image reveals considerable structure in the lobes, the position-velocity diagrams of the three polar spectra are spectrally quite smooth. In all three, a ridge of emission is seen in each lobe and at about the same position in each, ∼1″.8 from the central source in the northwest lobe and ∼2″.4 in the southeast lobe. In the H_2 image (reproduced in Fig. 4*d*), bright clumps are seen at ∼1″.8 and ∼2″.6 in the northwest lobe and ∼2″.2 and ∼2″.9 in the southeast lobe. Thus, these clumps are not resolved in the spectra, but appear as approximately weighted emission ridges. Of the three polar spectra, the emission appears strongest in the south (R) spectrum and weakest in the north (L) spectrum. The extent of the emission at the 20% contour level is 3″.0–3″.5 in the northwest lobe and 3″.8–4″.2 in the southeast lobe.

The H_2 velocity widths are approximately 34 km s^{-1} at the 50% contour level and 42 km s^{-1} at the 20% contour level for both lobes in all three polar spectra. The northwest and southeast lobes differ in velocity by only a few km s^{-1}, consistent with the nebula lying nearly in the plane of the sky. The average systemic velocity is $V_r = 11 \pm 1$ km s^{-1}.

The south (R) polar spectrum shows an additional strong emission component that lies at ∼1″.0 northwest of the stellar position. This component can be seen clearly in Figure 3, where it appears "ear shaped" and lies outside of the lobes, on the west side of the northwest lobe. This feature is significant, both because its velocity is ∼17 km s^{-1} redward of the nebula center, indicating motion into the plane of the sky, and because it has a velocity width only approximately half that of the polar lobes.

The spectra reveal that there is very little H_2 emission from the region near the central star (see Fig. 4*e*). The total velocity extent of the H_2 is comparable to that in the lobes, but here it comes from several distinct, narrow components. A weak component lies toward the nebula center, blueshifted by about 15 km s^{-1}.
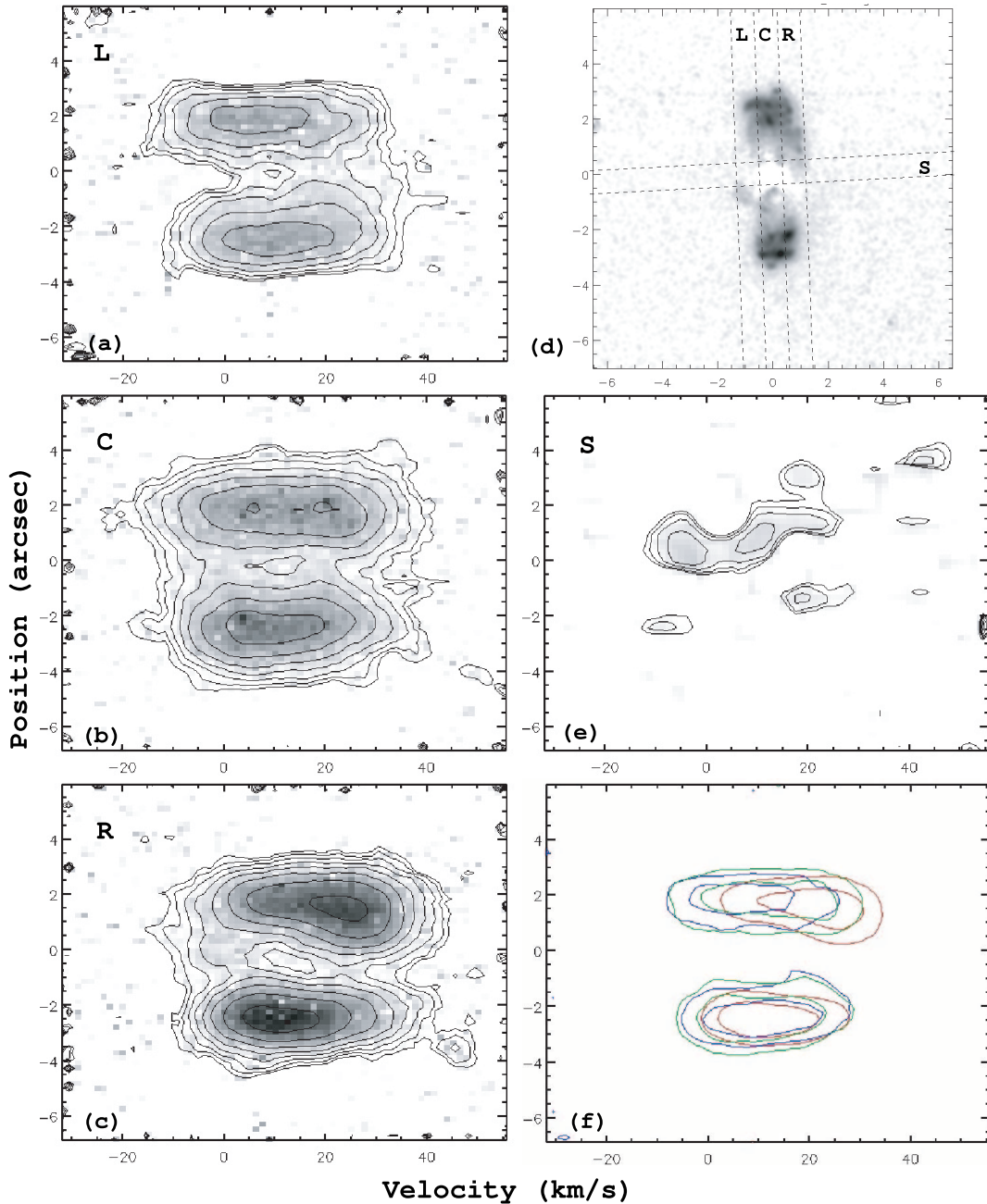
FIG. 4.—Position-velocity plots of IRAS 17150−3224 based on the high-resolution H₂ spectra observed at the four different slit positions: (*a*) north (L); (*b*) central (C); (*c*) south (R); and (*e*) stellar (S). Positive positions in (*a*)–(*c*) are along the northwest lobe and in (*e*) is toward the southwest. In (*d*) is reproduced (cf. Fig. 3*b*), for comparison, the H₂ image with the slits' positions, scaled to the position-velocity plots. In (*f*) is shown a composite figure with two contours at relatively high brightness levels (50% and 80% of the maximum of each) for each of the three polar spectra. They are color coded as follows: blue = L; green = C; red = R.

A somewhat weaker component lies to the southwest (+ position), close to the rest velocity of the nebula, and a faint component lies to the northeast (− position), redshifted by about 10 km s^{-1}.

If one compares the velocities of the emission peaks in the northwest and southeast lobes, an interesting trend appears. In the north (L) polar spectrum, the velocity of the northwest lobe is slightly (∼4 km s^{-1}) more negative than that of the southeast lobe, and in the central (C) one the lobe velocities are relatively similar, while in the south (R) spectrum, the velocity of the northwest lobe is slightly (∼6 km s^{-1}) more positive than that of the southeast lobe. In an overplot of the three polar position-velocity diagrams (Fig. 4*f*), one sees that the velocities in the southeast lobe are relatively similar (difference ≤1 km s^{-1}), but

in the northwest lobe the difference is substantial, ∼10 km s^{-1}, with the north side shifted 5 km s^{-1} to the blue and the south side shifted 5 km s^{-1} to the red relative to the nebula center.

Davis et al. (2005) have recently also made spatially resolved high-resolution ($R \sim 20,000$ or 16 km s^{-1}) H₂ observations of IRAS 17150−3224 (along with three other PPNs). Their observations were made with the slit oriented along the axis, through the bipolar lobes and passing through the star, and then offset 0″8 on either side of the bipolar axis, using a slit size of 0″8. Thus their slit positions are similar to ours, although their spectral resolution is ∼3 times lower. The position-velocity data in their study are very similar to ours, except that their labeling of the northeast and southwest spectra appears to be reversed compared

to ours. We have confirmed the correctness of our slit positions by rechecking the recorded pointing of the telescope.

5. DISCUSSION

The spectrum shows H_2 rotational-vibrational emission arising from three different transitions. The H_2 transitions $1-0$ $S(1)$ and $2-1$ $S(1)$ have a ratio of line strengths of 14 ± 3. This large ratio and the absence of higher excitation transitions ($\nu > 2$) indicate that the H_2 is collisionally excited (see Kelly & Hrivnak 2005),[8] with a vibration temperature of 1900 ± 130 K. Davis et al. (2003) obtained 2 μm spectra of IRAS $17150-3224$ at low resolution ($R \sim 400$), which covered a larger wavelength range of $1.92-2.22$ μm. They detected several additional H_2 lines and from them determined a rotational temperature of ~ 1300 K. They conclude that the nebula is primarily shock excited, but suggest a small contribution by fluorescence. The large velocity width (~ 35 km s^{-1}) seen in our high-resolution spectra, along with the H_2 intensity and deduced temperature, suggest collisional excitation in a C-type shock.

Shocks can be classified as "C-type" or "J-type" depending, respectively, on whether the density, temperature, and gas velocity vary smoothly across the shock front, or if they change discontinuously. C-type shocks are only possible if the transverse magnetic field strength in the preshock gas exceeds a critical value (cf. Draine 1980) that depends on the shock velocity, the preshock density, and the ionization. In C-type shocks, ion-neutral collisions accelerate the gas ahead of the shock front, resulting in an extended warm area, typically about 10^{17} cm in size, with neutral gas temperatures of $1000-2000$ K (Wilgenbus et al. 2000). In J-type shocks, the heat is deposited in a region of order 10^{13} cm in size and temperatures rise above $10,000$ K, resulting in rapid dissociation of H_2 and comparatively weak H_2 emission.

The H_2 emission in IRAS $17150-3224$ is strong, the emission region is $\sim 10^{16}$ cm in extent (see below), and the H_2 vibration temperature is only 1900 K, all of which point toward excitation in a C-type shock. In C-type shock models, the width of the H_2 lines at the 20% level appears to be comparable to the shock velocity (e.g., Davis et al. 2005; O'Connell et al. 2004). For IRAS $17150-3224$, this implies a shock velocity of about 40 km s^{-1}.

C-type shocks require that a magnetic field be present. Observations of strong circular polarization in OH 1665 MHz maser line by Hu et al. (1993) indicate the presence of a magnetic field in this object, and they calculate a field strength of $B \approx 300 \pm 150$ μG in the OH masing region. We compared the $1-0$ $S(1)$ line intensity and vibrational temperature to the magnetohydrodynamic models of Le Bourlot et al. (2002) and Wilgenbus et al. (2000). In their grids of models, they assumed that the magnetic field strength in microgauss was equal to the square root of the hydrogen density per cubic centimeter. For a shock velocity of 40 km s^{-1}, our line strength and vibrational temperature are consistent with a density of 10^4 cm^{-3} and a field strength of 100 μG. The data are also reasonably consistent with a shock velocity of 35 km s^{-1} and a density of 2×10^4 cm^{-3}.

For an assumed distance to IRAS $17150-3224$ of 2.4 kpc (Davis et al. 2005), the $1-0$ $S(1)$ line flux corresponds to a population of 1.65×10^{50} molecules in the upper level of the transition. Combined with the vibration temperature of 1900 K,

this indicates a total population of warm H_2 in the excited region of 1.2×10^{-5} $M_\odot$. At that distance, an observed clump size of $0.''3$ corresponds to a physical size of roughly 10^{16} cm. The expected dissociation rate in the postshock gas is only of order 10^{-13} s^{-1}, for a 40 km s^{-1} C-type shock propagating into a medium of $n_H = 10^4$ cm^{-3} and $B = 100$ μG (Wilgenbus et al. 2000), which corresponds to a lifetime of 3×10^5 yr. Given the rapid evolution of PPNs, most of the H_2 in the polar caps should survive until it is photodissociated at early B spectral types (Kelly & Hrivnak 2005).

H_2 emission in IRAS $17150-3224$ is seen to arise primarily from clumps near the ends of the bipolar lobes, with some general emission coming from the lobes and some weak emission from around the equatorial region (both loops, via H_2 imaging, and a blueshifted component, via high-resolution spectra). This is in contrast with AFGL 2688, in which strong emission was detected both from clumps near the ends of the lobes, and from the edges of a region extending out from the equator or "waist" of the nebula (Sahai et al. 1998). Both emission regions in the AFGL 2688 are shock excited (Sahai et al. 1998). The relatively weaker H_2 emission from the waist in IRAS $17150-3224$ likely arises because it has a less massive molecular torus; its torus is observed to be optically thin at 2 μm, while the torus in AFGL 2688 is optically thick out to at least 10 μm (Hora et al. 1996; Skinner et al. 1997).

The high resolution polar spectra show a systematic difference in the velocity of the lobes between the northeast (L) and southwest (R) sides. This is particularly the case in the northwest lobe, where the L spectrum appears to be shifted by about 5 km s^{-1} to the blue and the R spectrum by about 5 km s^{-1} to the red relative to nebula center. Two interpretations are advanced for this effect. The first is rotation of the nebula around the polar axis. This was previously suggested by Davis et al. (2005), who explore this as a possible signature of a magneto-centrifugal disk wind. As mentioned above, there exist observations of the OH 1665 MHz maser line showing strong circular polarization in this object, indicating the presence of a magnetic field (Hu et al. 1993). A second interpretation is that these differences arise from the motion of individual clumps slightly into or out of the plane of the sky. Given the roughly $10°$ opening angle of the lobes, shifts of this magnitude could be caused by tilts of the emitting clumps by this amount into or out of the plane of the sky.

Weintraub et al. (1998) have also obtained very high-resolution spectra ($\sim 100,000$ or ~ 3 km s^{-1}) of IRAS $17150-3224$ (AFGL 6815S) in the region of the H_2 $1-0$ $S(1)$ emission feature at 2.12 μm, although with lower S/N. They used a slit size of $1.''4 \times 60''$, oriented through the center of the nebula and aligned in the east-west direction (P.A. $= 90°$). They found double-peaked H_2 emission arising near the central region. They interpreted this as expanding molecular gas present in an equatorial torus, with an expansion velocity of ± 11 km s^{-1}. As noted in our description of the spectrum of the equatorial slit position, a blueshifted component is present. However, we do not see a redshifted one (unless we consider the fainter component $1.''3$ northeast of the central position), but we do see a component at the systemic velocity. Our higher spatial-resolution spectra do not support the idea of an expanding or a rotating torus close to the central star.

One can usefully compare the images of the nebulae in visible ($\sim V$) and near-infrared ($\sim H$) scattered light with the image in H_2 emission. This is done in Figure 5. The broadband visible and especially the near-infrared images show limb brightening in the lobes of IRAS $17150-3224$. This implies that they are low-density cavities, such as would be created by collimated
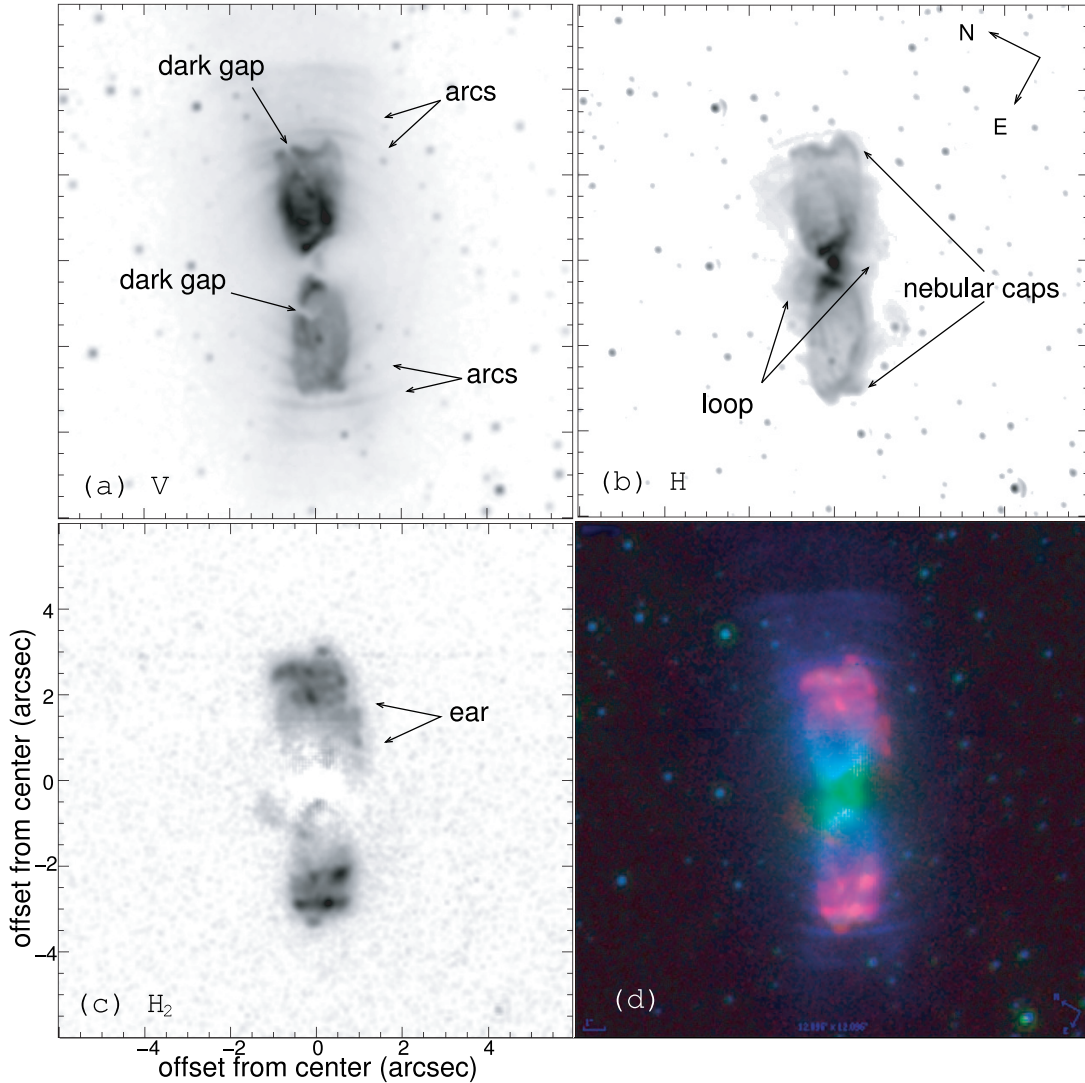
---

[8] It is possible to obtain such a high H_2 $1-0$ $S(1)$ to $2-1$ $S(1)$ line ratio by radiative excitation in a region of high gas density, $n > 10^6$ cm^{-3}, and high far-UV flux, $G_0 > 3 \times 10^4$ in units of the local interstellar field (Burton et al. 1990). However, these conditions, especially the high far-UV flux, do not appear to be present around this G2 central star.

Fig. 5.—Images of IRAS 17150−3224 at various wavelengths: (a) F606W (∼V band; $\lambda_{\rm eff} = 0.603$ μm, $\langle \Delta\lambda \rangle = 0.150$ μm); (b) F160W (∼H band; $\lambda_{\rm eff} = 1.593$ μm, $\langle \Delta\lambda \rangle = 0.277$ μm); and (c) H₂ emission (Fig. 6b). Panel d is a color composite of the three, with blue representing the V band, green the H band, and red the H₂ emission.

outflows. The "cap" structures at the ends of the lobes indicate that the cavities are not open cone-like regions, but rather have closed ends. This is consistent with the H₂ emission, which comes from clumps near the ends of the lobes. We interpret the clumpy H₂ emission as arising in the interaction zone of a collimated fast outflow colliding with the remnant of the preceding AGB wind.

The one region of H₂ emission that is hard to explain is the region southwest of the northwest lobe (the ear-shaped region on the outside right edge of the lobe, see Figs. 5c, and 5d). This appears to be outside the lobe wall. It has a high velocity (+17 km) relative to the system. This might represent a high-velocity outflow that has penetrated the lobe wall and excited H₂ in the surrounding remnant AGB medium.

A comparison of the H₂ emission image with the visible and near-infrared continuum images reveals some of the complexities in the nebula. In visible light (Fig. 5a), the northwest (top) lobe is brighter than the southeast lobe by a factor of 2, and slightly larger. In the near-infrared image (H-band; Fig. 5b), the southeast lobe is redder. (Also, Davis et al. [2003], from a study of H₂ line strengths, found the K-band extinction to be low in the northwest lobe and significantly higher in the southeast lobe.)

Taken together, and assuming general symmetry in the two lobes, these would suggest that the northwest lobe was tipped toward us and that light from the southeast lobe was subject to extra extinction that dimmed and reddened it. However, in the near-infrared image and in the H₂ image, the southeast lobe is larger, which at least is inconsistent with the idea that the two lobes are basically identical. If the northwest lobe were tipped toward us, it would be expected to show a blue shift in its spectrum relative to the southeast lobe, but this is not the case. The H₂ kinematical information indicates that the two lobes are nearly in the plane of the sky. Based on all of this information, we conclude that the polar axis is essentially in the plane of the sky, but that the two lobes differ in their brightness, either because of intrinsic difference in the lobes themselves or differences in the surrounding remnant AGB medium.

6. SUMMARY

This combined spectroscopic and imaging study of IRAS 17150−3224 has allowed us to determine the spatial location of the H₂ emission, which arises primarily from clumps near the ends of the lobes, and to also determine the excitation mechanism, which is collisional shocks. These shocks can arise when

the collimated fast outflow collides with the remnant of the AGB wind. Hence, the fast collimated outflow not only gives birth to the asymmetry in the circumstellar dust shell, creating the bipolar reflection nebula, but it also triggers the shock-excited molecular emission. The central star of IRAS 17150−3224, with a spectral type of G2, is in an earlier evolutionary phase than that of AFGL 2688 (F5). Therefore IRAS 17150−3224 provides direct evidence that the fast wind begins relatively early in the post-AGB evolution of these transitional objects. While our study does not reveal the cause of the torus around the star, it does document the action of the fast wind in shaping the lobes in a young PPN.

APPENDIX

SCALING THE NARROW-BAND IMAGES TO PRODUCE AN H_2 IMAGE

As discussed briefly in § 3, we investigated several different ways to calculate the appropriate scale factor to use in subtracting the flux-calibrated F215N image from the flux-calibrated F212N image. (The process of flux calibration has the effect of scaling the F215N image by a factor of 1.0512 relative to the F212N image prior to subtraction.) One could simply form the H_2 image by subtraction of the flux-calibrated images with no additional scaling if the source spectrum had the same spectral shape as the one used for calibration in this wavelength range, i.e., the same color. The resulting image formed by this scaling is shown in Figure 6a.
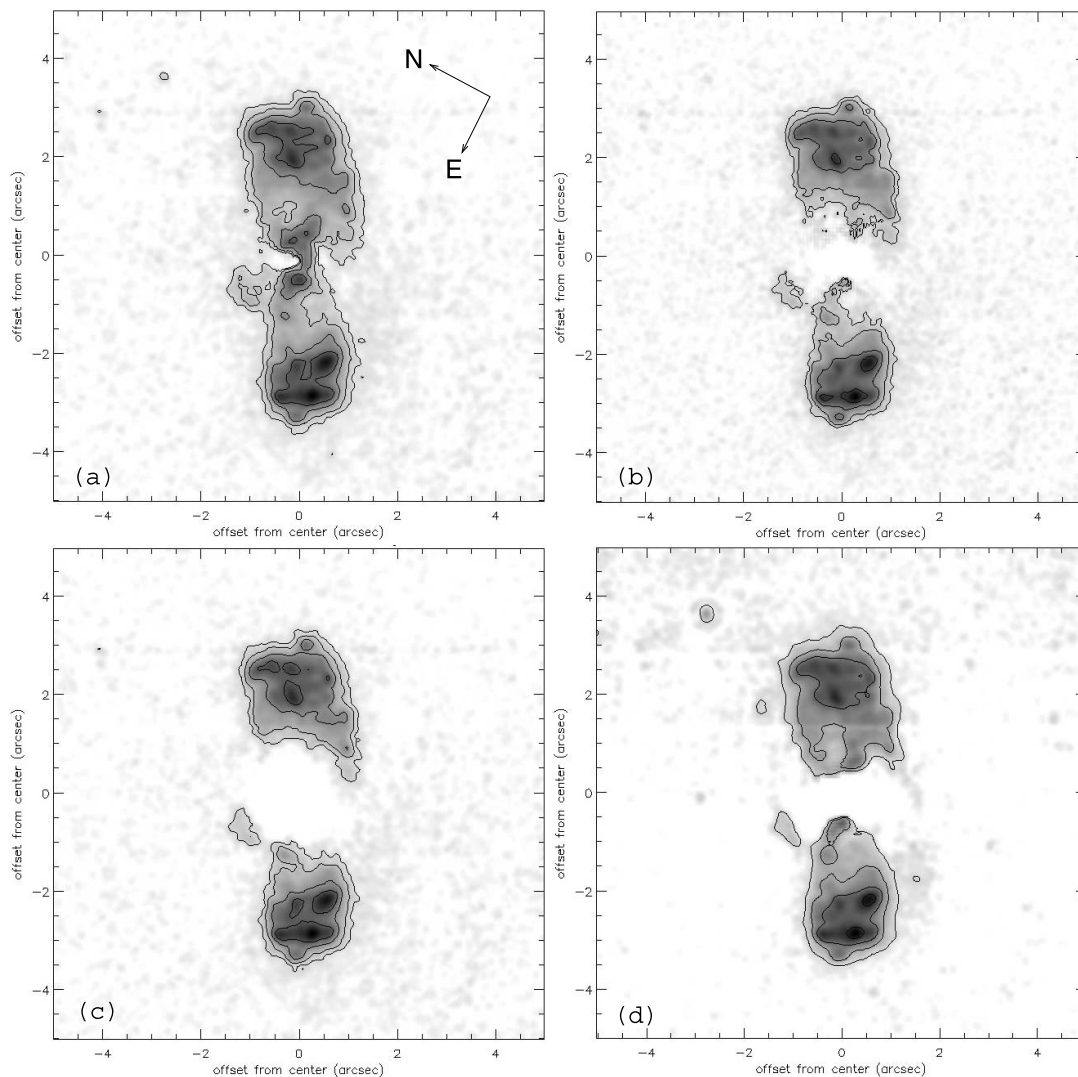

FIG. 6.—Various flux-calibrated, continuum-subtracted H_2 images of IRAS 17150−3224 with contours overlaid on the gray-scale color: (a) F212N−F215N (simply flux calibrated); (b) F212N − 1.0242 × F215N (scale factor based on the shape of 2 μm spectrum); (c) F212N − 1.045 × F215N (scale factor based on field stars); (d) F212N − 0.13082 × F222M (scale factor based on the shape of 2 μm spectrum). Overlaid contours are at flux-density levels of 5, 10, 20, 50, and 100 σ of detection (σ based on background variation in the resultant images). While the region around the central star varies among the various images, it can be seen that the H_2 emission in the lobes is very similar.

To include the correction for a different spectral shape, we examined several different ways to calculate an appropriate scale factor to use for the adjacent continuum image. We first convolved the fitted spectral continuum (with all the emission and absorption lines removed; see § 2) with the filter profiles and the detector response using STSDAS SYNPHOT calcphot task (the filter profiles in relationship to the spectrum are shown in Fig. 1). This resulted in a scale factor of 1.0242 due to the spectral shape. The resulting image formed by subtracting the flux-calibrated F215N image scaled by 1.0242 from the flux-calibrated F212N image is shown in Figure 6b. We also investigated a second scaling method, which was to determine a scale factor based on the observed flux ratio of the field stars in the two flux-calibrated images. This yielded a scale factor of 1.045 ± 0.015, based on eight field stars. This method assumes that the spectrum of the field stars is the same as that of the PPN in this spectral region and that the field stars emit no H$_2$ emission. This result is shown in Figure 6c. These two slightly different scaling methods are based on attempts to correct for the spectral shape of the central star in the nebula (first method) or the spectral shape of the field stars in the image (second method), the latter of which are apparently bluer than the light from the (reddened) central star. It can be seen that both of these methods to correct for the spectral shape result in the region around the star and between the lobes possessing a negative flux density, suggesting that it is slightly oversubtracted.

The continuum light from the nebula should actually be bluer than the central star, since it is light scattered by dust in the nebula and since the light from the central star is reddened in passing through the dense central region (torus). Thus, to correct for the nebula continuum flux would lead to a scaling factor slightly larger than the 1.0242 derived based on the spectral shape of the central star.

Although the resulting H$_2$ emission in the region around the star and between the two lobes varies among the different methods investigated above, the results are quite similar in the nebula. Figure 3a shows the H$_2$ image (scaled for the spectral shape of the central star, cf. Fig. 6b), with the approximate slit position of the FSpec spectrograph superimposed. Integrating the results of the H$_2$ emission within this slit area for the three cases investigated above results in H$_2$ fluxes of 8.0, 5.8, and 5.1 × 10^{-14} ergs cm^{-2} s^{-1} for the scale factors of 1.0000 (no scaling), 1.0242 (scaling for the color of the central star), and 1.0450 (scaling to the field stars), respectively, with the differences due to the amount of flux present in the region close to the star. These are all reasonably close to the observed (§ 2) value, now more properly scaled by the fact that only about 92% of the K-band flux is calculated to pass through the FSpec slit, of 7.2 × 10^{-14} ergs cm^{-2} s^{-1}.

The resulting emission levels in the nebula are not critically sensitive to which of these three reasonably chosen scale factors is used to subtract the continuum image. The total integrated emission flux within a circular aperture (radius of 1″) containing the bright clumps in the southeast lobe (see Fig. 3a) is 4.3, 4.2, 4.1 × 10^{-14} ergs cm^{-2} s^{-1} for the scale factors of 1.0000, 1.0242, and 1.0450, respectively, with less than 3% variation among the three cases. These scale factors all give approximately the same results for the distribution of the H$_2$ emitting regions and for the observed fluxes, apart from differences in the region around the star where most of the continuum flux originates. The high-resolution spectra (§ 4) show that little H$_2$ emission originates near the star.

We also investigated a fourth method of subtracting the continuum, this time using the medium-band K filter (F222M; $\lambda_{\rm eff} = 2.216$ μm, $\langle \Delta \lambda \rangle = 0.120$ μm). Proceeding as we did above, the images were first flux-calibrated (PHOTFLAM), which has the effect of scaling the F222M image by 0.13082. Convolving the fitted observed spectrum with the filter profiles and the detector response yielded a scaling factor of 1.0921. The resulting image formed by subtracting the scaled flux-calibrated F222M image from the flux-calibrated F212N image is shown in Figure 6d. It appears rather similar to Figure 6b, the image similarly formed using a scale factor based on the fitted spectral shape of the central star. The quantitative measurements of the emission in this image arising within the two regions delineated in Figure 3a both fall within the range of values found for the above three cases. Thus we conclude that with an observed spectrum for the source, the medium-band F222M image can also successfully (and efficiently) be used to subtract the continuum from the narrowband F212N image, as long as the H$_2$ emission region is extended enough to not be affected by the complex NICMOS point-spread function introduced by the use of the broader filter.

REFERENCES

Balick, B. 1987, AJ, 94, 671
Balick, B., & Frank, A. 2002, ARA&A, 40, 439
Blöcker, T. 1995, A&A, 299, 755
Burton, M. G., Hollenbach, D. J., & Tielens, A. G. G. M. 1990, ApJ, 365, 620
Cox, P., Huggins, P. J., Maillard, J.-P., Muthu, C., Bachiller, R., & Forveille, T. 2003, ApJ, 586, L87
Davis, C. J., Smith, D. M., Gledhill, T. M., & Varricatt, W. P. 2005, MNRAS, 360, 104
Davis, C. J., Smith, D. M., Stern, L., Kerr, T. H., & Chiar, J. E. 2003, MNRAS, 344, 262
Draine, B. T. 1980, ApJ, 241, 1021
García-Hernández, D. A., Manchado, A., García-Lario, P., Domínguez-Tagle, C., Conway, G. M., & Prada, F. 2002, A&A, 387, 955
Hinkle, K. H., Cuberly, R. W., Gaughan, N. A., Heynssens, J. B., Joyce, R. R., Ridgway, S. T., Schmitt, P., & Simmons, J. E. 1998, Proc. SPIE, 3354, 810
Hora, J. L., Deutsch, L. K., Hoffmann, W. F., & Fazio, G. G. 1996, AJ, 112, 2064
Hu, J. Y., Slijkhuis, S., Nguyen-Q-Rieu, & de Jong, T. 1993, A&A, 273, 185
Kastner, J. H., Weintraub, D. A., Gatley, I., & Henn, L. 2001, ApJ, 546, 279
Kastner, J. H., Weintraub, D. A., Gatley, I., Merrill, K. M., & Probst, R. G. 1996, ApJ, 462, 777
Kelly, D. M., & Hrivnak, B. J. 2005, ApJ, 629, 1040
Koekemoer, A. M., et al. 2002, HST Dither Handbook (Ver. 2.0; Baltimore: STScI)

Kwok, S. 1982, ApJ, 258, 280
Kwok, S., Hrivnak, B. J., Zhang, C. Y., & Langill, P. L. 1996, ApJ, 472, 287
Kwok, S., Su, K. Y. L., & Hrivnak, B. J. 1998, ApJ, 501, L117
Latter, W. B., Dayal, A., Bieging, J. H., Meakin, C., Hora, J. L., Kelly, D. M., & Tielens, A. G. G. M. 2000, ApJ, 539, 783
Le Bourlot, J., Pineau des Forêts, G., Flower, D. R., & Cabrit, S. 2002, MNRAS, 332, 985
O'Connell, B., Smith, M. D., Davis, C. J., Hodapp, K. W., Khanzadyan, T., & Ray, T. 2004, A&A, 419, 975
Sahai, R., Hines, D. C., Kastner, J. H., Weintraub, D. A., Trauger, J. T., Rieke, M. J., Thompson, R. I., & Schneider, G. 1998, ApJ, 492, L163
Sahai, R., Sanchez Contreras, C., & Morris, M. 2005, ApJ, 620, 948
Sahai, R., & Trauger, J. T. 1998, AJ, 116, 1357
Schneider, G., & Stobie, E. 2002, ASP Conf. Ser. 281, Astronomical Data Analysis Software and Systems XI (San Francisco: ASP), 382
Skinner, C. J., et al. 1997, A&A, 328, 290
Su, K. Y. L., Hrivnak, B. J., & Kwok, S. 2001, AJ, 122, 1525
Su, K. Y. L., Hrivnak, B. J., Kwok, S., & Sahai, R. 2003, AJ, 126, 848
Ueta, T., Meixner, M., & Bobrowsky, M. 2000, ApJ, 528, 861
Weintraub, D. A., Huard, T., Kastner, J. H., & Gatley, I. 1998, ApJ, 509, 728
Wilgenbus, D, Cabrit, S., Pineau des Forets, G., & Flower, D. R. 2000, A&A, 356, 1010